Available online at www.sciencedirect.com
ScienceDirect
International Journal of Heat and Mass Transfer 51 (2008) 1854–1865
International Journal of HEAT and MASS TRANSFER
www.elsevier.com/locate/ijhmt

Extended heat-transfer relation for an impinging laminar flame jet to a flat plate

M.J. Remie [a], G. Särner [b], M.F.G. Cremers [a], A. Omrane [b], K.R.A.M. Schreel [a], M. Aldén [b], L.P.H. de Goey [a,*]

[a] Eindhoven University of Technology, Department of Mechanical Engineering, P.O. Box 513, 5600 MB Eindhoven, The Netherlands
[b] Lund Institute of Technology, Division of Combustion Physics, P.O. Box 118, SE-221 00 Lund, Sweden

Received 2 January 2007; received in revised form 6 June 2007
Available online 1 October 2007

Abstract

Many industrial applications use flame impingement to obtain high heat-transfer rates. An analytical expression for the convective part of the heat transfer of a flame jet to a plate is derived. Therefore, the flame jet is approximated by a hot inert jet. In contradiction with existing convective heat-transfer relations, our analytical solution is applicable not only for large distances between the jet and the plate, but also for close spacings. Multiplying the convective heat transfer by a factor which takes chemical recombination in the cold boundary layer into account, results in an expression for the heat flux from a flame jet to the hot spot of a heated plate. Numerical and experimental validation show good agreement.

Keywords: Impinging flame jet; Heat transfer; Oxy-fuel; Phosphorescence

1. Introduction

Flame-impingement heating is a frequently employed method to enhance the heat transfer to a surface. Applications can for instance be found in the glass industry, where glass products are melted, cut and formed using impinging flame jets. It is well reckoned that these jets yield very high heat-transfer coefficients [1–4]. Experiments have been performed concerning the heat-transfer characteristics of impinging flame jets as well [5–10].

The flame jets are operated in a laminar as well as a turbulent configuration. Turbulent flame jets can particularly be found in glass furnaces. When the jets are used in smaller geometries to apply the heat locally, however, the flames will be laminar. These flows are highly viscous because of their high temperatures. Since these flames are laminar, mixing of ambient air causing a temperature decrease of the flame is suppressed.

The main heat-transfer mechanism for impinging flame jets is forced convection. Radiation from the flame is negligible because of the very low emissivity of a hot gas layer of small thickness [11,1,12]. In the last few decades it became more accepted to increase the amount of oxygen in the oxidizer stream. Enhancing the amount of oxygen in the flame jet results in a higher flame temperature and a higher burning velocity. Not only the convective heat transfer will now be increased, another heat-transfer mechanism called Thermochemical Heat Release (TCHR) will start to play an important role as well [12]. The oxygen-enhanced flames contain a lot of free radicals such as O, H and OH. When the flame impinges on the cold surface of the heated glass product, the radicals will recombine in the boundary layer resulting in an increased heat transfer. Cremers [13–15] found that the heat transfer coefficient of a methane–oxygen and a hydrogen–oxygen flame can be as much as doubled compared to a chemically frozen mixture. Baukal and Gebhart [16] experimentally found

* Corresponding author. Fax: +31 40 2433445.
E-mail address: l.p.h.d.goey@tue.nl (L.P.H. de Goey).

0017-9310/$ - see front matter © 2007 Elsevier Ltd. All rights reserved.
doi:10.1016/j.ijheatmasstransfer.2007.06.042

Nomenclature

Roman characters

a	applied strain rate (1/s)
c_p	specific heat at constant pressure (J/(kg K))
g	gravitational acceleration (m/(s^2))
H	flame tip-to-plate distance (m)
H^*	critical distance (m)
h	heat-transfer coefficient (W/(m^2 K))
K	strain rate of the burnt gases (1/s)
$\dot{m}$	mass flux (kg/(m^2 s))
m	mass (kg)
Nu	Nusselt number (–)
Pe	Peclet number (–)
Pr	Prandtl number (–)
$\mathscr{P}$	pressure tensor (N/m^2)
p	pressure (N/m^2)
q	heat flux (W/m^2)
R	burnt gas jet radius (m)
Re	Reynolds number (–)
Ri	Richardson number (–)
s_L	laminar burning velocity (m/s)
T	temperature (K)
TCHR	TCHR factor (–)
t	time (s)
U	uniform flow velocity (m/s)
u, v	velocity components (m/s)
$\mathbf{u}$	velocity field (m/s)
$\mathbf{v}$	velocity field (m/s)
x_δ	viscous boundary layer thickness (m)
x, r	cylindrical coordinates (m)

Greek symbols

α	thermal diffusivity (m^2/s)
β	velocity gradient (1/s)
λ	thermal conductivity (W/(m K))
μ	dynamic viscosity (kg/(m s))
ν	kinematic viscosity (m^2/s)
ρ	density (kg/m^3)
τ	expansion coefficient (–)
τ	stress tensor (kg/(m s^2))

Abbreviations

CFD	computational fluid dynamics
ICCD	intensified charge-coupled device
MFC	mass flow controller
PMT	photomultiplier tube
TCHR	thermochemical heat release

this result as well. Furthermore, they concluded that the peak heat flux for these flames occurs at the stagnation point. This is in contrast with fuel-air flames, where the peak heat flux is shifted away from the stagnation point.

The flow behaviour of flame jets and hot isothermal jets is comparable. According to Viskanta [1], the aerodynamics of a single flame jet is very similar to the aerodynamics of a single isothermal jet. Experiments by van der Meer [11] showed that the axial velocity decays slightly faster for the flame jets than for the isothermal jets, due to the axial temperature decay. The radial velocity gradients at the stagnation point are found to be equal.

Simple analytical expressions for the heat transfer of inert jets are very useful from an engineering point of view when the heat transfer needs to be estimated. Sibulkin derived a semi-analytical relation for the laminar heat transfer of an impinging flow to a body of revolution [17]. This relation has been the basis of most other experimental and theoretical results since [18–22]. An important limitation of this relation, however, is that it is only applicable for large nozzle-to-plate spacing. Nevertheless, smaller spacing becomes very interesting when the heat flux needs to be increased. Furthermore, for the limit of non-viscous flows an unrealistic heat transfer is predicted using this model. In an earlier study [23] we presented an analytically derived expression for the convective heat flux of a hot inert jet. With this expression it is possible to predict a realistic heat flux for the limit of non-viscous flows. On the other hand, it is only applicable for small nozzle-to-plate spacing. In this paper we will present an extension of the analytical expression, which will be valid for small as well as large nozzle-to-plate spacing. Because of the resemblance in flow behaviour between flame jets and hot isothermal jets, we will focus on hot inert flame jets in the rest of the paper.

First we will show how the analytical expression for the heat flux of a hot inert flame jet, applicable for small nozzle-to-plate distances, is derived. With this expression the local heat flux to the hot spot of the plate can be calculated. The solution is also applicable for a closely staggered array of jets. The derivation is performed for an axi-symmetrical case by solving the conservation equations taking only the most important contributions into account. Since it is not possible to find the full analytical solution, the results will be validated by numerical calculations. Using the numerical results, an extension of the analytically derived expression can be derived to make it valid for large nozzle-to-plate spacing as well. Finally we will show the results of temperature measurements of a quartz plate which was heated by a methane–oxygen as well as a hydrogen–oxygen flame. The experiments were carried out to validate the analytically and numerically obtained heat-transfer expressions.

2. Analytical solution for the heat transfer

Fig. 1 shows a schematic overview of a premixed stagnation flame impinging normal to a plane surface. From this

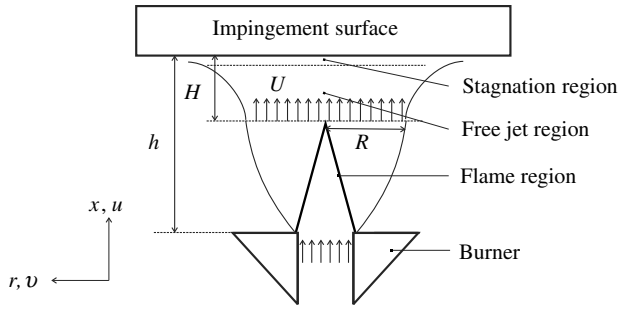

Fig. 1. Schematic overview of a stagnation flame impinging to a plane surface.

figure, we can distinguish the flame region, the free jet region, the stagnation region and the impingement surface. Cremers [13] has shown that since the typical time scales of the regions are different, the regions can be decoupled, treated separately and coupled afterwards again. We will focus on the free jet region and the stagnation region to calculate the heat flux from the flame to the hot spot of the plate, which has a width of $2R$. For a flame where pure oxygen is supplied to the oxidizer stream, Remie [24] has shown that the burnt gases form a flow profile very close to a plug flow after the flame front. The velocity of the burnt gases rapidly drops at the edges of the stream tube. The resulting plug flow velocity U [m/s] and plug flow jet radius R [m], which can be calculated using the unburnt gas parameters [24], will be used as input parameters for the model.

In literature often the distance from the burner to the impingement surface h [m] is used as an independent parameter. However, using different fuels while keeping the unburnt gas velocity constant results in different flame heights because of the different burning velocities. Therefore, if the distance from the burner to the plate h is kept constant, the distance from the flame tip to the plate H [m] will vary for the different fuels. For this reason, we choose the distance from the flame tip to the plate H as an input parameter, instead of the distance from the burner to the plate h.

First we will consider the case where the plate is positioned close to the flame tip, $H \leqslant R$. A hot inert plug flow with velocity U and burnt gas jet radius R, which is formed after the flame front, impinges on the plate. The system now is reduced to a steady one-dimensional problem and behaves as a potential flow far from the surface. A thin boundary layer of thickness x_δ is formed close to the surface. The heat-transfer processes induce a fast temperature change in the boundary layer. We will analyse the system by studying the transport equations in both regions and coupling the solutions at the edge of the regions.

The conservation equations of mass and momentum are given by

$$\frac{\partial \rho}{\partial t} + \nabla \cdot (\rho \mathbf{v}) = 0, \tag{1}$$

$$\frac{\partial (\rho \mathbf{v})}{\partial t} + \nabla \cdot (\rho \mathbf{v}\mathbf{v}) = -\nabla \cdot \mathscr{P} + \rho \mathbf{g}, \tag{2}$$

where $\mathbf{g}$ is the gravitational vector [m/s^2] and the tensor $\mathscr{P}$ is a short-hand notation for $\mathscr{P} = p\mathbf{I} + \tau$. Furthermore, p is the hydrostatic pressure [Pa], $\mathbf{I}$ the unit tensor and τ the stress tensor [kg/(m s^2)].

Often the Richardson number Ri is used to determine the importance of buoyancy in the flow. The Richardson number is a dimensionless number that expresses the ratio of potential to kinetic energy. Since $Ri = \mathscr{O}(10^{-5})$ in this case, the effect of buoyancy is neglected. The jet is inert, since we approximate the flame jet by a hot isothermal jet and take no chemical recombination into account. To calculate the total heat flux, the convective heat flux can simply be multiplied by a factor which takes the thermochemical heat release into account [13]. Since the core region of the jet flow is essentially one-dimensional, the temperature is a function of the spatial coordinate x only, so $T = T(x)$ and therefore $\rho = \rho(x)$. Assuming an incompressible flow and using the ideal gas law $p = \rho RT$, ρT is a constant. Since the velocity profile is a plug flow, the velocity component u is a function of x only. Using $\dot{m} = \rho u$ and $v = r \cdot \hat{v}(x)$, the continuity equation now yields

$$\frac{\mathrm{d}\dot{m}}{\mathrm{d}x} = -\rho K, \tag{3}$$

where K, the strain rate of the mixture [1/s], is a function of x only and equal to $K = 2\hat{v} = 2\partial v/\partial r$.

If $p = p(x,r)$ and $\mu = \mu(x)$, the equations for x- and r-momentum become [25,26]:

$$-\dot{m}\frac{\mathrm{d}u}{\mathrm{d}x} + \frac{\mathrm{d}}{\mathrm{d}x}\left[\frac{2}{3}\mu\left(2\frac{\mathrm{d}u}{\mathrm{d}x} - K\right)\right] + \frac{\mu}{2}\frac{\mathrm{d}K}{\mathrm{d}x} = \frac{\partial p}{\partial x}, \tag{4}$$

$$\dot{m}\frac{\mathrm{d}K}{\mathrm{d}x} + \frac{1}{2}\rho K^2 - \frac{\mathrm{d}}{\mathrm{d}x}\left(\mu\frac{\mathrm{d}K}{\mathrm{d}x}\right) = -\frac{2}{r}\frac{\partial p}{\partial r}, \tag{5}$$

with μ the dynamic viscosity [kg/(m s)]. It can be seen from Eq. (4), that the pressure derivative $\partial p/\partial x$ is a function of x only. Differentiation of equation (4) with respect to r and changing the order of differentiation then gives that $\partial p/\partial r$ is a function of r only. From Eq. (5) it then follows that $-2\partial\, p/(r\partial r)$ is a constant, i.e.

$$\dot{m}\frac{\mathrm{d}K}{\mathrm{d}x} - \frac{\mathrm{d}}{\mathrm{d}x}\left(\mu\frac{\mathrm{d}K}{\mathrm{d}x}\right) = J - \frac{1}{2}\rho K^2 \tag{6}$$

with $J = -2\partial p/(r\partial r)$. The strain rate K increases as the flow approaches the plate to a maximum at the plate for non-viscous flows. For viscous flows the maximum strain rate is a bit smaller due to the viscous boundary layer than for non-viscous flows. Now the maximum strain rate can be found not at the plate but, due to the viscous boundary layer, close to the plate. At the plate, the strain rate will be equal to zero. If we define the maximum strain rate $a = K_{\max}$ [1/s], for non-viscous flows J becomes equal to $\rho_b a^2/2$, with ρ_b the density of the burnt gases. For viscous flows J will not be equal to $\rho_b a^2/2$, but the difference is assumed to be small.

Eq. (6) cannot be solved analytically for the whole domain $-H < x < 0$, where $x = -H$ is the position of the

flame tip and $x = 0$ is the flame side of the plate. An analytical solution can be obtained, however, if we decouple the domain in a region far from the plate to the viscous boundary layer, $-H < x < -x_\delta$, and a region consisting of the viscous boundary layer, $-x_\delta < x < 0$. The resulting solutions for the velocity profiles in both regions will be linked at $x = -x_\delta$, where $K = a$.

The order of magnitude for the terms of equation (6) far from the plate can be estimated using $\mathcal{O}(x) = H$ and $\mathcal{O}(K) = U/H$:

$$\mathcal{O}\left(\rho\frac{U^2}{H^2}\right) + \mathcal{O}\left(\mu\frac{U}{H^3}\right) = \mathcal{O}(\rho a^2) + \mathcal{O}\left(\rho\frac{U^2}{H^2}\right). \tag{7}$$

Since $\mathcal{O}(a) = U/H$, it is easy to see that the viscous term is not relevant far from the plate if $H \gg \sqrt{\nu/a}$, where $\nu = \mu/\rho_b$ is the kinematic viscosity [m^2/s].

Far from the plate the density is constant. Using the continuity equation (3), the relation between the strain rate K and the velocity u becomes:

$$K = -\frac{\mathrm{d}u}{\mathrm{d}x}. \tag{8}$$

Using Eq. (8), Eq. (6) is now reduced to:

$$-uu'' = \frac{1}{2}a^2 - \frac{1}{2}u'^2. \tag{9}$$

The solution for this equation can be obtained analytically. The boundary conditions at $x = -H$ are $u = U$ and $K = -\mathrm{d}u/\mathrm{d}x = 0$. Using these boundary conditions, the following solutions for the velocity profile and strain profile can be found:

$$u(x) = -\frac{a^2}{4U}(x + x_{\mathrm{ref}})^2 - a(x + x_{\mathrm{ref}}), \tag{10}$$

$$K(x) = \frac{a^2}{2U}(x + x_{\mathrm{ref}}) + a, \tag{11}$$

where $a = 2U/H$ and the value of x_{ref} is determined by the boundary layer thickness x_δ. Eqs. (10) and (11) are valid for $-H < x < -x_\delta$, but also for the whole domain if the flow is non-viscous ($x_{\mathrm{ref}} = 0$).

Close to the plate $\dot{m}$ and K become zero and Eq. (6) is reduced for $-x_\delta < x < 0$ to

$$-\frac{\mathrm{d}}{\mathrm{d}x}\left(\mu\frac{\mathrm{d}K}{\mathrm{d}x}\right) = \frac{1}{2}\rho_b a^2 \tag{12}$$

indicating a quadratic behaviour as function of x for K in the viscous boundary layer. In this region, the density and velocity of the burnt gas flow can be approximated by

$$\rho \sim \rho_0 + \rho' x, \quad u \sim bx^2$$

with ρ_0 the density of the burnt gas flow at the flame side of the plate and b a constant. Eq. (8) still holds, since

$$\rho\frac{\mathrm{d}u}{\mathrm{d}x} \sim 2b\rho_0 x, \quad u\frac{\mathrm{d}\rho}{\mathrm{d}x} \sim b\rho' x^2,$$

and therefore $\rho\mathrm{d}u/\mathrm{d}x \gg u\,\mathrm{d}\rho/\mathrm{d}x$. Now, using $K(0) = 0$ and $K(-x_\delta) = a \simeq 2U/H$, the solution for the velocity profile in the viscous boundary layer becomes

$$u(x) = ax_\delta\left(\frac{x^3}{3x_\delta^3} + \frac{x^2}{x_\delta^2}\right) \tag{13}$$

with $x_\delta = 2\sqrt{\nu/a}$. The velocity profile far from the plate (10) will be coupled to the velocity profile in the viscous boundary layer (13) at $x = -x_\delta$, where $K = a = 2U/H$. Eq. (10) for $-H < x < -x_\delta$ now becomes:

$$u(x) = -\frac{a^2}{4U}(x + x_\delta/3)^2 - a(x + x_\delta/3). \tag{14}$$

Convection and thermochemical heat release are the main heat-transfer mechanisms for impinging oxy-fuel flame jets. To calculate the convective contribution, the conservation equation of energy for the burnt gasses close to the heated side of the plate is reduced to a balance of conduction and convection:

$$\rho u c_p\frac{\mathrm{d}T}{\mathrm{d}x} = \frac{\mathrm{d}}{\mathrm{d}x}\left(\lambda\frac{\mathrm{d}T}{\mathrm{d}x}\right). \tag{15}$$

where c_p is the heat capacity of the burnt gas flow [J/(kg K)] and λ the conductivity coefficient [W/(m K)]. Substituting the equations for the velocity u (13) and (14) results in relations for the heat transfer from the burnt gas flow to the wall.

First we determine the heat transfer for a non-viscous gas flow ($x_\delta = 0$). We assume both λ and the thermal diffusivity $\alpha = \lambda/(\rho c_p)$ [m^2/s] to be constant. Numerical calculations have shown that this assumption is valid. After substituting $q = \lambda\,\mathrm{d}T/\mathrm{d}x$, the conservation equation of energy (15) changes to:

$$\int_s^0 \frac{\mathrm{d}q}{q} = \frac{1}{\alpha}\int_s^0 u\,\mathrm{d}x, \tag{16}$$

which after integration results in the following equation for q:

$$q(s) = q_0\exp\left[-\frac{1}{\alpha}\int_s^0 u\mathrm{d}x\right]. \tag{17}$$

Now we introduce the Peclet number, a dimensionless parameter giving the ratio of heat transfer by convection and conduction. The Peclet number is defined as $Pe = UH/\alpha$. Eq. (17) can be made dimensionless using $x' = x/H$. After integration over the whole domain $-H < x < 0$ and substituting Eq. (14) for the velocity profile u, the solution for the non-viscous heat transfer from the burnt gases to the plate q_0 is given by

$$q_0 = \lambda\frac{\mathrm{d}T}{\mathrm{d}x}\Big|_0 = \frac{\lambda(T_0 - T_{\mathrm{flame}})}{\int_{-H}^0 \exp\left[-\frac{1}{\alpha}\int_s^0 u\mathrm{d}x\right]\mathrm{d}s} \tag{18}$$

$$= \frac{\lambda(T_0 - T_{\mathrm{flame}})}{H\int_{-1}^0 \exp\left[-Pe\left(\frac{1}{3}x'^3 + x'^2\right)\right]\mathrm{d}s'}. \tag{19}$$

If we take viscosity into account to calculate the heat flux q_0, we have to make the distinction between the burnt gas flow region and the viscous boundary layer again to calculate the denominator of equation (18). The denominator of equation (18) now becomes equal to

$$\begin{aligned}&\int_{-H}^{0}\exp\left[-\frac{1}{\alpha}\int_{s}^{0}u\mathrm{d}x\right]\mathrm{d}s\\&=\int_{-x_\delta}^{0}\exp\left[-\frac{1}{\alpha}\int_{s}^{0}u_2\,\mathrm{d}x\right]\mathrm{d}s\\&\quad+\int_{-H}^{-x_\delta}\exp\left[-\frac{1}{\alpha}\left(\int_{s}^{-x_\delta}u_1\mathrm{d}x+\int_{-x_\delta}^{0}u_2\,\mathrm{d}x\right)\right]\mathrm{d}s,\end{aligned}\quad(20)$$

where the velocity profile in the burnt gas flow region u_1 is given by Eq. (14) and the velocity profile in the viscous boundary layer u_2 by Eq. (13). Implementing these velocity profiles in Eq. (20) and making this equation dimensionless, results in the following denominator for Eq. (18) for the viscous situation:

$$\begin{aligned}&\int_{-H}^{0}\exp\left[-\frac{1}{\alpha}\int_{s}^{0}u\mathrm{d}x\right]\mathrm{d}s\\&=H\int_{-x_\delta/H}^{0}\exp\left[\frac{1}{12}\frac{Pe^2}{Pr}x'^4+\sqrt{\frac{4}{18}\frac{Pe^3}{Pr}}x'^3\right]\mathrm{d}s'\\&\quad+H\int_{-1}^{-x_\delta/H}\exp\left[-Pr-Pe\left(\frac{1}{3}x'^3+\frac{1}{3}\sqrt{\frac{2Pr}{Pe}}x'^2+\frac{1}{9}\frac{2Pr}{Pe}x'\right.\right.\\&\quad\left.\left.+\frac{1}{9}\sqrt{\frac{2Pr}{Pe}}^3+x'^2+\frac{2}{3}\sqrt{\frac{2Pr}{Pe}}x'-\frac{1}{3}\frac{2Pr}{Pe}\right)\right]\mathrm{d}s'.\end{aligned}\quad(21)$$

With this equation, the convective heat flux for a hot (flame) jet to a target can be calculated, if the jet is placed close to the target.

3. Numerical results

The previous section showed the analytical solution for the convective heat transfer of a hot inert flame jet to the hot spot of a plate, if the jet is positioned close to the plate, $H \leqslant R$. Some assumptions had to be made, in order to be able to perform the analytical derivation. In this paragraph we will check whether these assumptions hold and validate the results of the analytical solutions by comparing them with numerical solutions. The numerical solutions are obtained using Fluent [27]. Fluent is a CFD (Computational Fluid Dynamics) package with which it is possible to carry out a numerical analysis and generate solutions of flow and heat-transfer problems. Fluent uses a finite volume method and the flow calculations are based on the solution of the Navier–Stokes equations.

Fig. 2 shows the model we used in Fluent to perform the calculations. A hot inert plug flow with a temperature of $T = 3000$ K, a velocity of $U = 75$ m/s and a radius R enters the domain. The plate is modelled as a wall, which has a fixed temperature of $T = 300$ K and a width of $10R$, in order to minimize the effect of the pressure outflow boundary at the right side of the domain on the plug flow. The left side of the domain is modelled as a symmetry axis. At both pressure boundaries, the derivatives of velocity and temperature are equal to zero. Both the flow and temperature fields are solved.

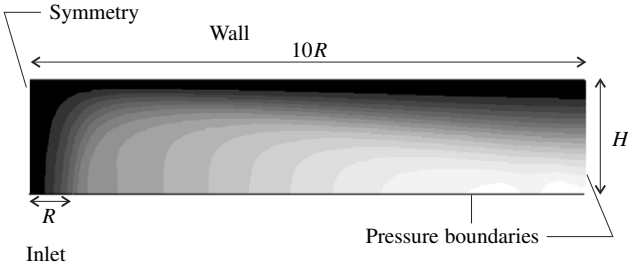

Fig. 2. Schematic overview of the Fluent model. The different grayscales represent the streamlines.

The simplifications used for the transport coefficients in the analytical model are also used in the numerical solution. The parameters of the burnt gases are chosen to be constant with $\rho = \rho_b = 0.083$ kg/m^3, $c_p = 2000$ J/(kg K), $\mu = 5.6\,10^{-5}$ kg/(m s) and $\lambda = 0.16$ W/(m K). The values for c_p, λ and μ are chosen at a temperature of 1500 K using Chem1D [28] and the thermodynamic data from the GRI-mech 3.0 mechanism.

First we check whether the strain rate K, defined by Eq. (3), can be simplified according to Eq. (8). Therefore $u\partial\rho/\partial x$ should be significantly smaller than $\rho\partial u/\partial x$. Fig. 3 shows both terms as a function of the distance to the plate. For this particular calculation a temperature dependent density was used, namely $\rho = 1.1\,(T/298)^{-1.06}$ [28]. The figure shows that far from the plate $u\frac{\partial\rho}{\partial x} = 0$. Closer to the plate $u\frac{\partial\rho}{\partial x}$ is not negligible anymore, but $\rho\frac{\partial u}{\partial x}$ still is the leading term. Therefore, the assumption seems to hold.

The analytical solution for the velocity of the burnt gases was obtained by solving the momentum equation in

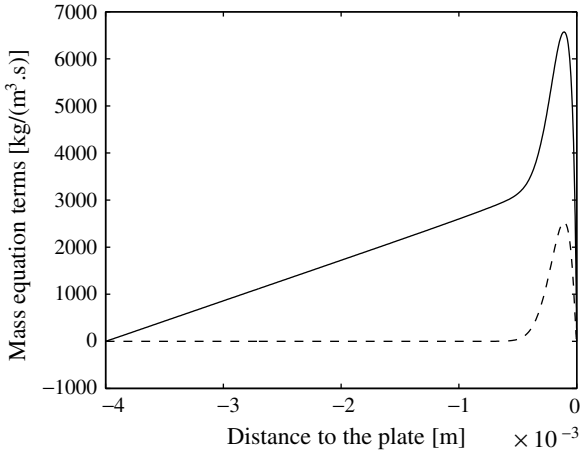

Fig. 3. The terms $-\rho\frac{\partial u}{\partial x}$ (solid line) and $u\frac{\partial\rho}{\partial x}$ (dashed line) plotted against the distance to the plate x, with $U = 75$ m/s, $T = 3000$ K, $H = 4$ mm and $R = 20$ mm.

r-direction. Therefore a distinction was made between the burnt gas region far from the plate where the diffusivity term was neglected and the viscous boundary layer where the convection term and the source term were assumed to approach zero. In Fig. 4 the separate terms of equation (6) are plotted against x. Far from the wall, the viscous term indeed is not relevant and therefore there is a balance between the convection term, the source term and the constant $\rho_b a^2$. Very close to the wall, the convection term and the source term become zero and the negative diffusion term equals the constant $\rho_b a^2$. The solutions for the velocity profiles far from the wall and in the viscous boundary layer close to the plate were linked together at $x = -x_\delta$, which is approximately at $x = -0.2$ mm. At $x = -x_\delta$ there is a balance between the four terms, which is not taken into account in the derivation of the analytical solution. The results of the numerical calculations will show whether this approximation has a big influence on the velocity profile.

Eqs. (13) and (14) represent the analytical solution for the velocity profile from the symmetry axis up to close to the edge of the stream tube when $H < R$. Fig. 5 shows a comparison between this analytical solution (dashed line) and the numerical results obtained with Fluent (solid line). The analytical equations for the velocity profile correspond very well to the numerical calculations.

Eq. (19) represents the convective heat flux from the inert flame jet to the hot spot for the non-viscous case. The heat flux for the viscous case can be calculated using Eqs. (18) and (21). The temperature profile over the symmetry axis is calculated with Fluent. The resulting heat flux to the hot spot, using $q = \lambda \frac{\partial T}{\partial x}|_0$, can be compared with the analytical solution. The heat transfer is calculated for different Prandtl numbers Pr, ranging from 0 (non-viscous flow) to 1.

The ratio of the analytically calculated heat flux and the non-viscous heat flux as a function of Pr is depicted using

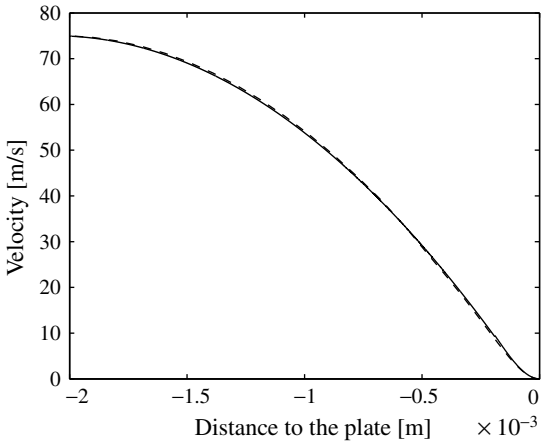

Fig. 5. Velocity profile over the symmetry boundary, with $U = 75$ m/s, $T = 3000$ K, $H = 2$ mm and $R = 20$ mm. The dashed line represents the analytical calculation, the solid line represents the numerical results.

dots in Fig. 6. The asterisks represent the ratio of the numerically calculated heat flux and the non-viscous heat flux as a function of Pr. Therefore a distance to the plate of $H = 2$ mm and a plug width of $R = 20$ mm are chosen. For a Prandtl number of 0, the ratio between the viscous heat transfer and non-viscous heat transfer should be equal to 1. A small deviation can be observed for the numerical results. For increasing Prandtl number, the heat transfer should decrease due to an increasing viscous boundary layer thickness. A good agreement can be observed between the analytical and numerical results.

It is expected that the heat transfer to the plate shows a fast decay outside the hot spot, which is defined as the part of the surface at the wall from $r = 0$ to $r = 2R$. Also, the heat flux within the hot spot will decrease with increasing distance from the symmetry plane due to the gases which flow radially outwards. To check the validity range of the analytical equations for the heat flux (18) and (21), the

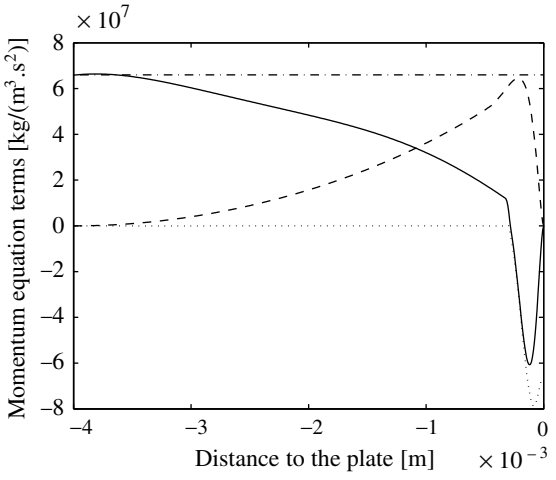

Fig. 4. The separate terms of equation (6). The solid line represents the convection term $\dot{m}\frac{dK}{dx}$, the dotted line the diffusion term $\frac{d}{dx}(\mu\frac{dK}{dx})$, the dashed line the source term ρK^2 and the dashed-dotted line the constant term $\rho_b a^2$, with $U = 75$ m/s, $T = 3000$ K, $H = 4$ mm and $R = 20$ mm.

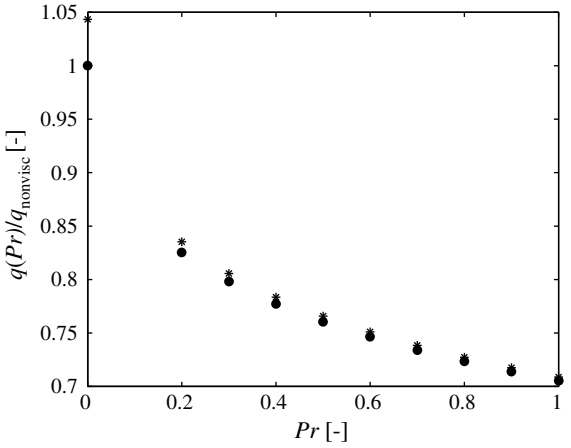

Fig. 6. The ratio of the viscous heat flux and non-viscous heat flux as a function of the Prandtl number. The dots represent the analytical results, the asterisks the numerical results; $U = 75$ m/s, $T = 3000$ K, $H = 2$ mm, $R = 20$ mm.

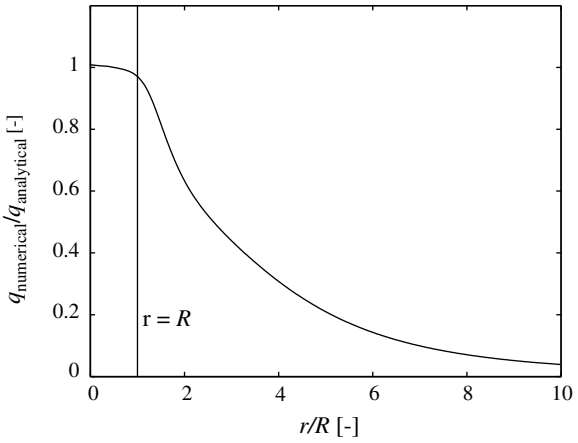

Fig. 7. Ratio of the numerically calculated heat flux and the analytical heat flux at the hot spot as a function of r/R.

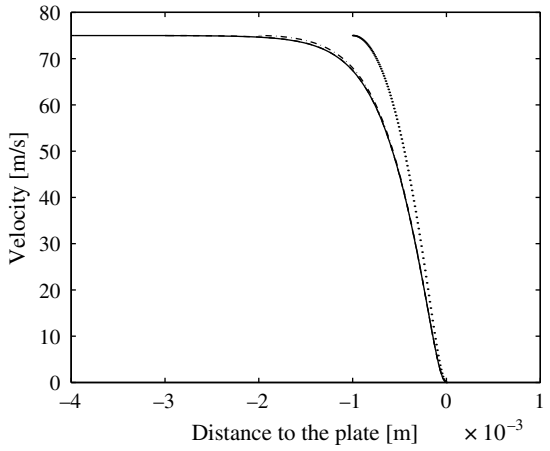

Fig. 8. Velocity profiles over the symmetry boundary, for the solid line $H = 4$ mm, for the dashed line $H = 3$ mm, for the dashed-dotted line $H = 2$ mm and for the dotted line $H = 1$ mm.

local heat flux over the entire plate is calculated using Fluent.

Fig. 7 shows the ratio of the numerically calculated local heat flux as a function of the normalized distance to the symmetry axis r/R, and the constant analytical heat flux at the hot spot, given by Eq. (18). The ratio of the numerical and analytical heat flux is equal to 1 at the symmetry axis. A small decrease can be observed with increasing distance from the symmetry plane to the edge of the hot spot at a normalized distance of $r/R = 1$. The heat transfer decreases fast outside the hot spot. Therefore, the analytical solutions for the heat flux seem to hold for the hot spot region.

4. Solution for $H > R$

So far we derived the convective heat flux from a hot inert jet to the hot spot of the plate if the plate is positioned close to the jet, $H < R$. It was observed that the maximum strain rate $a = K_{max}$ just before the plate determines the heat flux. For small flame tip to plate distances, the strain rate is given by $a = 2U/H$. Increasing the gas velocity U or decreasing the distance from the flame tip to the plate H will result in a larger strain rate. Because of the increased strain rate, the boundary layer will be thinner and therefore the heat flux will be increased.

Increasing the distance from the flame tip to the plate H while keeping the gas velocity U constant will have the opposite effect. The strain rate decreases and therefore the heat flux will decrease as well. From a certain distance from the flame tip to the plate, however, the boundary layer will reach its maximum thickness and the maximum strain rate will remain constant. The maximum strain rate is no longer equal to $a = 2U/H$ from this point on. This effect is visualized in Fig. 8. This figure shows the velocity profiles over the symmetry plane for a plug flow with radius $R = 0.5$ mm and an increasing flame tip to plate distance from 1 to 4 mm. Increasing the distance from $H = 1$ (dotted line) to 2 mm (dashed-dotted line) results in a thicker boundary layer and therefore a smaller strain rate. Increasing the distance to $H = 3$ mm only has little effect on the velocity profile, while increasing the distance from $H = 3$ to 4 mm has no effect at all. Therefore, increasing the distance to the plate has no effect on the velocity profiles for high H/R ratios and the strain rate will remain constant. We will show in this section how the strain rate and therefore the heat flux alters for the case that $H > R$ using the results of Fluent calculations.

The numerical effect of the ratio H/R on the maximum strain rate a is shown in Fig. 9. The factor $aH/(2U)$ is plotted as a function of H/R. This factor is equal to *1* for small values of H/R; this is in agreement with the analytical solution. Keeping the distance to the plate H and the burnt gas velocity U constant and decreasing the plug flow radius R results in an increase of the effective strain rate a. Furthermore, for a H/R ratio of 4 and higher and a constant plug flow radius R and burnt gas velocity U, the distance to the plate H has no influence on the strain rate a. The strain rate

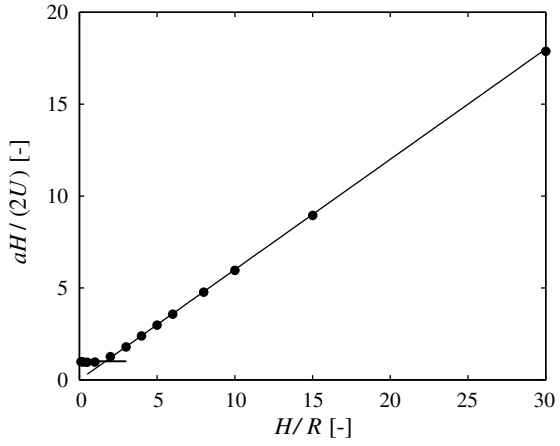

Fig. 9. Relation between $aH/(2U)$ and H/R; the dots represent the numerical calculations, the solid lines the functions $aH/(2U) = 1$ and $aH/(2U) = 18H/(30R)$.

a now is a constant, represented by the straight line indicating that $aH/(2U) \sim H/R$ or $a = 6U/(5R)$ independent of H.

We can now adjust Eq. (21) to make it valid not only for $H/R < 1$ but for the complete H/R range. The two straight lines in Fig. 9 intersect at $H/R = 5/3$. Since the strain rate is independent of the distance H for a ratio of H/R larger than 5/3, the strain rate for large H/R ratios can be defined as $a = 6U/(5R) = 2U/H^*$. The critical distance H^* is defined here as $H^* = 5R/3$. Eq. (21) now can be written as:

$$\begin{aligned}\int_{-H^*}^{0} \exp\left[-\frac{1}{\alpha}\int_{s}^{0} u\mathrm{d}x\right]\mathrm{d}s &= H^*\int_{-x_\delta/H^*}^{0}\exp\left[\frac{1}{12}\frac{Pe^2}{Pr}x'^4+\sqrt{\frac{4}{18}\frac{Pe^3}{Pr}}x'^3\right]\mathrm{d}s' \\ &+ H^*\int_{-1}^{-x_\delta/H^*}\exp\left[-Pr-Pe\left(\frac{1}{3}x'^3+\frac{1}{3}\sqrt{\frac{2Pr}{Pe}}x'^2\right.\right. \\ &\left.\left.+\frac{1}{9}\frac{2Pr}{Pe}x'+\frac{1}{9}\sqrt{\frac{2Pr}{Pe}}^3+x'^2+\frac{2}{3}\sqrt{\frac{2Pr}{Pe}}x'-\frac{1}{3}\frac{2Pr}{Pe}\right)\right]\mathrm{d}s'\end{aligned} \tag{22}$$

with

$$H^* = \begin{cases} H & \text{for } H < 5R/3, \\ 5R/3 & \text{for } H \geqslant 5R/3, \end{cases} \tag{23}$$

and $Pe = U\,H^*/\alpha$.

Fig. 10 shows the results for the heat flux q as a function of the distance from the flame tip to the plate H for a plug flow radius of $R = 1$, 2, 3, 4 and 6 mm (solid lines). The figure shows that for values of the distance $H < 5R/3$, the plug flow radius has no influence on the heat flux. For values of the distance $H \geqslant 5R/3$, however, the heat flux is no longer dependent of the distance H but becomes dependent of the plug flow radius R. Numerical validations for $R = 1$, 2 and 3 mm (asterisks) show very good agreement.

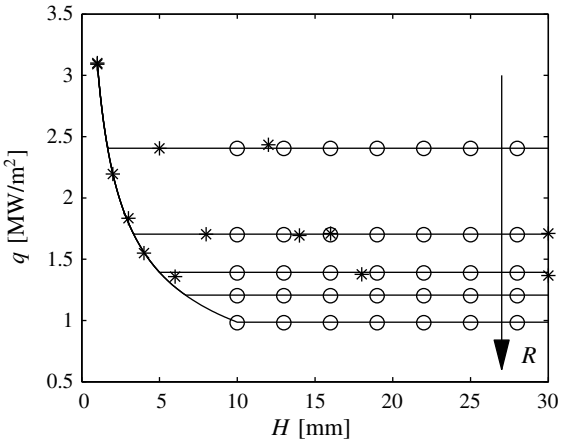

Fig. 10. Convective heat flux as a function of the flame top-to-plate distance H for burnt gas flow tube radii of $R = 1,2,3,4$ and 6 mm. The solid lines represent the analytical solutions, the asterisks the numerical solutions from FLUENT and the circles the results found according to Sibulkin.

Let us now compare the presented results with the well-known reference work of Sibulkin [17]. Sibulkin solved the boundary layer equations for laminar heat transfer to a body of revolution near the forward stagnation point. The body of revolution is assumed to be immersed in an infinite, laminar, incompressible, low-speed stream. For the Nusselt number in the stagnation point he found:

$$Nu = 0.763\left(\frac{\beta}{\nu}\right)^{0.5} 2RPr^{0.4}, \tag{24}$$

where the Nusselt number is the ratio of convective to conductive heat transfer $Nu = h2R/\lambda$, with h the heat-transfer coefficient [W/(m K)]. The velocity gradient just outside the boundary layer is defined here as $\beta = (\partial v/\partial r)_{r=0}$, see Fig. 1. This solution is independent of the flame tip-to-plate spacing. Furthermore, it is only applicable for larger spacing ($H/R > 8$) [18]. Another characteristic of that solution is that for the limit of a non-viscous situation, an infinite Nusselt number and therefore an infinite heat transfer is predicted.

The heat flux according to Sibulkin can be calculated, using Eq. (24), with [21]:

$$q_0 = 0.763(\beta\rho\mu)^{0.5}Pr^{-0.6}c_p(T_{\text{flame}} - T_0). \tag{25}$$

The values of the gas parameters are chosen the same way as shown in the previous paragraph, so $\rho = \rho_b = 0.083$ kg/m^3, $c_p = 2000$ J/(kg K), $\mu = 5.6 \times 10^{-5}$ kg/(m s) and $\lambda = 0.16$ W/(m K). The temperature of the hot gases is set to 3000 K, while the temperature of the plate is fixed at 300 K. From potential flow solutions a value for the velocity gradient β for a circular disc is found [19,20] to be equal to $\beta = 2U/(\pi R)$. This velocity gradient is found for an infinite stream around a circular disc with radius R. Experiments show that the velocity gradient β for a disc with radius R in a uniform cross flow is the same as for a uniform jet with radius R impinging on a flat plate [11]. Since in our case a jet with finite width is impinging on an infinite plate, we use the radius of the jet to calculate the velocity gradient.

A comparison with our analytical model is shown in Fig. 10, where the results from Sibulkin are depicted with the circles. The results of the relation according to Sibulkin show very good agreement with the results of our analytical relation for large H/R spacings. The curve in the left part of the figure, representing the convective heat flux for small H/R spacings, is not found by Sibulkin. It can also be noted, looking at Eqs. (18) and (21), that with our relation for the heat transfer, a realistic heat flux can be calculated for low viscosity flows.

5. Experimental validation

The previous section showed that the analytical solution we derived for the convective heat flux from an inert jet to a plate shows good agreement with numerical calculations for small H/R ratios as well as large H/R ratios. Cremers

[15] has shown that the total heat flux, where the effect of TCHR is incorporated, can be calculated by multiplying the convective heat flux by a so-called TCHR-factor. This TCHR-factor mostly depends on the fuel of the flame, the temperature of the plate and the strain rate. Since measurements at the heated side of the plate are difficult to make due to the high temperature and velocity of oxy-fuel flames, experimental validations of the temperature have been performed on the other side of the plate. The quartz plate used for these experiments was heated by a methane–oxygen as well as a hydrogen–oxygen flame. The temperature increase inside a flat quartz plate is also calculated numerically by solving the instationary conduction equation with a convective heat flux multiplied by a TCHR-factor as a boundary condition. In this section the results of the calculations are compared with the experimentally obtained temperature increase as function of time of the back side of the plate to validate the model.

The measurement technique used for the measurements is based on phosphor thermometry. For a more detailed description of this technique, we refer the reader to Omrane [29], while a review article about phosphor thermometry written by Allison [30] is useful as well. In recent years this phosphorescence technique has been developed for remote measurements of surface temperature. It is based on measuring temperatures by seeding the material with a temperature-sensitive thermographic phosphor. Thermographic phosphors are ceramic materials doped with rare earth elements from which light is emitted. When the phosphor is excited by an appropriate light source, it becomes highly phosphorescent. The emission is typically in the visible region and has a lifetime of the order 10^{-3} s. This lifetime is temperature sensitive; therefore, measuring the decay of the phosphorescence is a measure for the temperature at any given time. As the phosphor coating thickness is usually less than 100 μm, the particles are assumed to reach thermal equilibrium with the investigated surface instantaneously.

A large number of phosphors is produced covering a large band of temperatures from cryogenic up to 2200 K. Each selected phosphor is very sensitive in a specific range, where an accuracy of the order 1–5 K is obtained. A big advantage is that the method is non-intrusive, therefore allowing the gas to move non-disturbed close to the surface. Furthermore, the phosphor has a fast response to thermal changes. Since the phosphor can survive in very harsh conditions, the technique has found use in different combustion related applications.

The thermographic phosphor Mg_3FGeO_4:Mn, Mn^{4+} being the activator, was used for the experiments. The Mn activator emits light originating only from electronic transition between the excited state $^4F_2$ and the ground state $^4A_2$, resulting in emission at 631 and 657 nm. The excitation lifetime is strongly temperature dependant as reported by Omrane [29]. Fig. 11 shows a schematic of the experimental set-up. The phosphor was coated to the surface using the non-fluorescent binder HPC found to

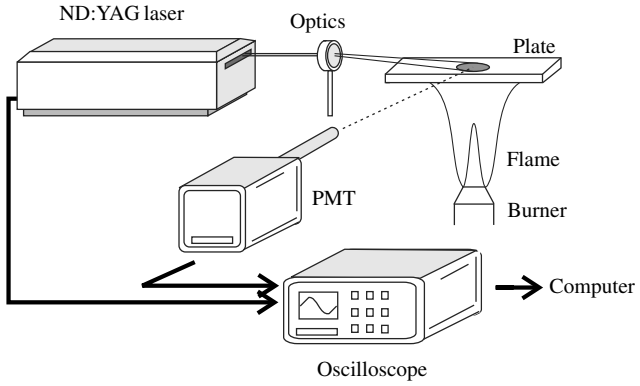

Fig. 11. Schematic overview of the experimental set-up consisting of a Nd:YAG laser, PMT, oscilloscope, optics and burner.

be suitable for harsh conditions [31]. Excitation of the phosphor was conducted using the third harmonic at 355 nm of an Nd:YAG laser with a pulse duration of 8 ns and a repetition rate of 10 Hz. A laser intensity of 8 mJ was used to obtain phosphorescence. The laser light was focused on the top side of a quartz plate directly above the hot spot, where the radius of the hot spot was equal to R, which is the radius of the burnt gas flow tube. The dimensions of the quartz plate were equal to $100 \times 100 \times 5$ mm. The part of the top side of the plate directly above the hot spot was coated with the phosphor. The subsequent emission was collected by a PhotoMultiplier Tube (PMT). A 3 GHz oscilloscope, triggered by the laser, was used to digitize the signal from the PMT. The measured emission decay was fitted to the theoretical model $I = I_0 \cdot \exp[-t/\tau]$ and compared to a calibration curve. Both a methane–oxygen and hydrogen–oxygen flame were used to heat the quartz plate. The premixed gas mixture was supplied to the burner using a mixing panel with Mass Flow Controllers (MFCs), which were set and monitored using an interface to a PC. The burner nozzle diameter was equal to $d = 1.7$ mm. Remie [24] has shown that the resulting radius of the burnt gas jet will be equal to $R = \tau^{0.5} \cdot d/2$, with τ the expansion coefficient. The different parameters for both flames are shown in Table 1. Since $\tau = 12.6$ for the methane–oxygen flames, $R = 3.0$ mm. For the hydrogen–oxygen flames with $\tau = 8.3$, $R = 2.4$ mm. The measurements were performed for an unburnt gas velocity of 70 m/s and flame tip-to-plate distances of $H = 2$, 5, 10 and 20 mm.

Fig. 12 shows a typical result of a temperature measurement of the quartz plate heated by a flame. For this measurement, a methane–oxygen flame was used with a gas velocity of $U = 70$ m/s and a flame tip-to-plate distance of $H = 10$ mm was set. After each measurement, the plate was cooled down to approximately 400 K before the next measurement was performed.

To calculate the heating curves numerically, the PDEPE solver of MATLAB [32] was used. This solver solves the instationary one-dimensional conduction equation for the heat transfer in the plate. Since quartz is a bad heat

Table 1
Values of different parameters of methane–oxygen and hydrogen–oxygen flames

	ρ_b (kg/(m^3 s))	λ (W/(m K))	c_p (J/(kg K))	μ (kg/(m s))	τ (–)	TCHR (–)
CH_4–O_2	0.083	0.16	2000	5.6×10^{-5}	12.6	2.0
H_2–O_2	0.059	0.30	2500	5.6×10^{-5}	8.3	2.0

The values are chosen at a temperature of 1500 K, with exception of the density of the burnt gases ρ_b and the expansion factor τ.

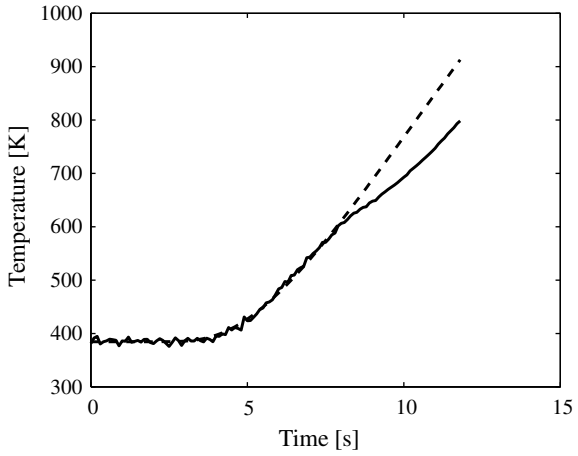

Fig. 12. Typical temperature increase of the back side of the quartz plate as a function of time. The plate was heated by a methane–oxygen flame, with $U = 70$ m/s and $H = 10$ mm. The solid line represents the results of the experiment, the dashed line the numerically obtained results.

conductor and the width of the burnt gas jet is approximately the same (hydrogen–oxygen flame) as or larger (methane–oxygen flame) than the thickness of the quartz plate (5 mm), the one-dimensional approach is assumed to suffice for at least the initial part of the heating process. The boundary condition at the front side is equal to a convective heat flux multiplied with a TCHR-factor to take the heat release into account which is released after the recombination of radicals at the cold plate surface. A value of 2.0 is chosen for the TCHR-factor for both flames, chosen at a temperature of 1500 K [15]. The values of the gas parameters are also chosen at a temperature of 1500 K, as was done in the previous section, see Table 1. An adiabatic boundary condition was set at the top side of the plate. Since only the initial part of the heating process is considered, radiation does not have to be taken into account. Remie [33] has shown that the heating of the quartz plate with temperature dependent λ, ρ and c_p is almost the same as the heating with temperature independent parameters, if the temperature independent λ is multiplied by a factor of 0.75. Therefore, the parameters of the quartz plate are chosen to be equal to $\rho = 2250$ kg/m^3, $c_p = 780$ J/(kg K) and $\lambda = 0.75 \times 1.4$ W/(m K) [34].

To be able to compare the numerically obtained heating curves with the experimentally obtained heating curves, a non-linear least squares fitting procedure is used. A good fitting requires that as few as possible parameters are varied. In this case, the most obvious choice is to vary the total heat-transfer coefficient h, the initial temperature and the point of time where the flame is ignited. A typical result of such a fit is shown in Fig. 12, where the numerical results of the heating of the cold side of the quartz plate are represented by the dashed line. Initially, a good agreement can be observed. After about 8 seconds, a deviation can be observed. At that time, the hot side of the plate got very hot resulting in a strong Planck radiation visible as a red glow. Therefore, thermal radiation leading to a too high DC level on the PMT could have interfered with the measurements, resulting in a non-linear response and thus too low temperatures in the evaluation. To minimize this affect, only a fit for the initial part of the heating was performed.

Using the fitting procedure, for every measurement a convective heat flux can be determined. It is also possible to calculate an analytical convective heat flux for each measured situation using (18) and (22). Let us now compare the analytically and experimentally obtained heat fluxes using a heat flux figure similar to Fig. 10.

Figs. 13 and 14 show the comparisons between the analytically obtained convective heat fluxes and the experimentally obtained convective heat fluxes for the methane–oxygen flame and the hydrogen–oxygen flame, respectively. The solid lines represent the analytical solutions for the heat flux, the circles the experimentally determined heat fluxes. The horizontal error bars are obtained by taking into account the inaccuracy of the manual set flame tip-to-plate distance H (0.2 mm, which is approximately the flame thickness). The vertical error bars are obtained by using a 95% confidence interval (2σ error) of the variance

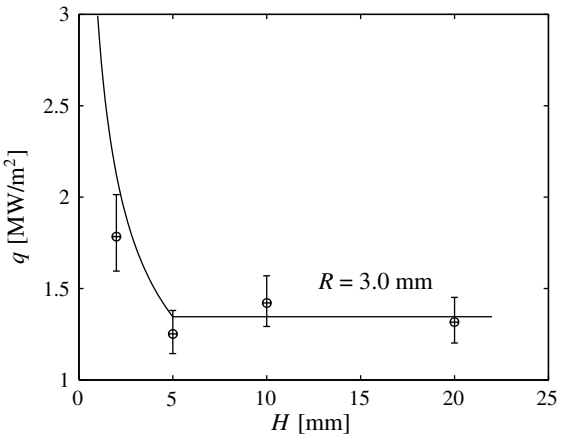

Fig. 13. Convective heat flux as a function of the flame tip-to-plate distance H for a burnt gas flow tube radius of $R = 3.0$ mm. The solid line represents the analytical solutions, the circles with errorbars the measurements with the methane–oxygen flame for $R = 3.0$ mm, $U = 70$ m/s and $H = 2$, 5, 10 and 20 mm.

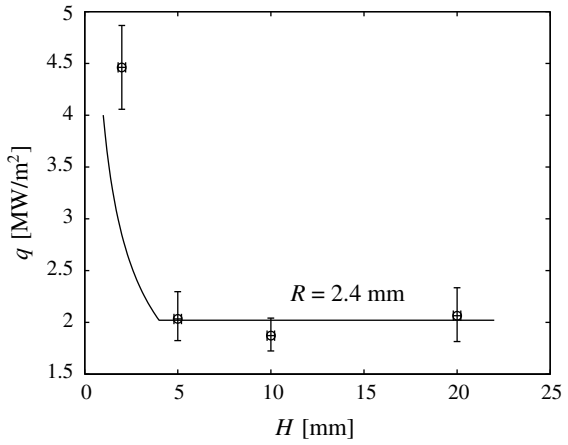

Fig. 14. Convective heat flux as a function of the flame tip-to-plate distance H for a burnt gas flow tube radius of $R = 2.4$ mm. The solid line represents the analytical solutions, the circles with errorbars the measurements with the hydrogen–oxygen flame for $R = 2.4$ mm, $U = 70$ m/s and $H = 2$, 5, 10 and 20 mm.

of the heat-transfer coefficient h. The figures show a good comparison between the analytical model and the experiments. Although the measurement with the hydrogen–oxygen flame at a distance of $H = 2$ mm does not precisely coincide with the analytical model, the figures clearly show that for large flame tip-to-plate distances, the heat flux remains constant. For small flame tip-to-plate distances, however, the heat flux will be very sensitive to small shifts in distance. The heat flux will increase rapidly if the plate is put closer to the plate.

6. Conclusions

In this paper we have shown how a relation for the convective heat flux from a hot inert jet to the hot spot of a plate can be derived analytically. In contradiction with existing relations for the convective heat flux, our solution is not only applicable for relative large distances from the jet to the plate, but also for the case that the jet is placed close to the plate. Furthermore, it is possible to obtain realistic solutions for low viscous flows.

The analytical expression is obtained by taking only the dominant terms of the conservation equation into account. Therefore, the flow is divided into two regions. The region far from the plate is treated as a potential flow where viscosity is neglected. In the region close to the plate, viscosity becomes a leading term. The solutions of the velocity profiles for both regions are coupled to each other at the edge of the viscous boundary layer. The energy equation is given by a balance between conduction and convection. The derived equations for the velocity profiles are inserted in the energy equation. After integration over the whole domain, the heat flux to the hot spot of the plate can be found.

Comparison with the existing relations for the convective heat transfer showed good agreement. The presented numerical calculations also proved the validity of the analytical model. The heat transfer from impinging flame jets to a plate can be calculated by multiplying the convective heat transfer from a hot inert jet to a plate with a Thermochemical Heat Release factor. This TCHR-factor accounts for the contribution of chemical recombination of radicals in the cold boundary layer. Phosphor thermometry measurements have been performed on a quartz plate heated by a methane–oxygen and a hydrogen–oxygen flame to validate the analytical model experimentally. The experimentally obtained convective heat fluxes show good agreement with the analytical model. The experiments clearly show that for large distances the heat flux is constant, while for short distances the heat flux becomes very sensitive for small shifts in distance.

Acknowledgement

The financial support by Philips Lighting B.V. is gratefully acknowledged.

References

[1] R. Viskanta, Heat transfer to impinging isothermal gas and flame jets, Exp. Thermal Fluid Sci. 6 (1993) 111–134.
[2] R. Viskanta, Convective and radiative flame jet impingement heat transfer, Int. J. Transport Phenom. 1 (1997) 1–15.
[3] C.E. Baukal, B. Gebhart, A review of flame impingement heat transfer studies – Part 1: Experimental conditions, Combust. Sci. Technol. 104 (1995) 339–357.
[4] C.E. Baukal, B. Gebhart, A review of flame impingement heat transfer studies – Part 2: Measurements, Combust. Sci. Technol. 104 (1995) 359–385.
[5] L.L. Dong, C.W. Leung, C.S. Cheung, Heat transfer of a row of three butane/air flame jets impinging on a flat plate, Int. J. Heat Mass Transfer 46 (2003) 113–125.
[6] L.L. Dong, C.W. Leung, C.S. Cheung, Heat transfer and wall pressure characteristics of a twin premixed butane/air flame jets, Int. J. Heat Mass Transfer 47 (2004) 489–500.
[7] L.C. Kwok, C.W. Leung, C.S. Cheung, Heat transfer characteristics of slot and round premixed impinging flame jets, Exp. Heat Transfer 16 (2003) 111–137.
[8] L.C. Kwok, C.W. Leung, C.S. Cheung, Heat transfer characteristics of an array of impinging pre-mixed slot flame jets, Int. J. Heat Mass Transfer 48 (2005) 1727–1738.
[9] Z. Zhao, T.T. Wong, C.W. Leung, Impinging premixed butane/air circular laminar flame jet – influence of impingement plate on heat transfer characteristics, Int. J. Heat Mass Transfer 47 (2004) 5021–5031.
[10] C.R. Kleijn, Heat transfer from laminar impinging methane/air flames, computational technologies for fluid/thermal/structural/chemical systems with industrial applications, ASME 1 (2001) 259–269.
[11] T.H. van der Meer, Heat transfer from impinging flame jets, Ph.D. thesis, Delft University of Technology, 1987.
[12] C.E. Baukal, B. Gebhart, Surface condition effects on flame impingement heat transfer, Exp. Thermal Fluid Sci. 15 (1997) 323–335.
[13] M.F.G. Cremers, M.J. Remie, K.R.A.M. Schreel, L.P.H. de Goey, Heat transfer mechanisms of laminar flames of hydrogen + oxygen, Combust. Flame 139 (2004) 39–51.
[14] M.F.G. Cremers, M.J. Remie, K.R.A.M. Schreel, L.P.H. de Goey, Thermochemical heat release of laminar stagnation flames of fuel and oxygen, Combust. Flame, under review.

[15] Marcel Cremers, Heat transfer of oxy-fuel flames to glass – the role of chemistry and radiation, Ph.D. thesis, Technische Universiteit Eindhoven, 2006, pp. 103–107.
[16] C.E. Baukal, B. Gebhart, Heat transfer from oxygen-enhanced/natural gas flames impinging normal to a plane surface, Exp. Thermal Fluid Sci. 16 (1998) 247–259.
[17] M. Sibulkin, Heat transfer near the stagnation point of a body of revolution, J. Aeronaut. Sci. 19 (1952) 570–571.
[18] P.S. Shadlesky, Stagnation point heat transfer for jet impingement to a plane surface, AIAA J. 21 (8) (1983) 1214–1215.
[19] W.M. Kays, Convective heat and mass transfer, McGraw-Hill, New York, 1966.
[20] V. Kottke, H. Blenke, K.G. Schmidt, Messung und Berechnung des ortlichen und mittleren Stoffübergangs an stumpf angestromten Kreisscheiben bei unterschiedlicher Turbulenz, Wärme und Stoffübertragung 10 (1977) 89–105.
[21] C.E. Baukal Jr, Heat Transfer in Industrial Combustion, CRC Press LLC, Boca Raton, 2000.
[22] J.K. Kilham, M.R.I. Purvis, Heat transfer from normally impinging flames, Combust. Sci. Technol. 18 (1978) 81–90.
[23] M.J. Remie, M.F.G. Cremers, K.R.A.M. Schreel, L.P.H. de Goey, Analysis of the heat transfer of an impinging laminar flame jet, Int. J. Heat Mass Transfer 50 (2007) 2816–2827.
[24] M.J. Remie, M.F.G. Cremers, K.R.A.M. Schreel, L.P.H. de Goey, Flame jet properties of Bunsen-type flames, Combust. Flame 147 (2006) 163–170.
[25] R.J. Kee, J.A. Miller, G.H. Evans, G. Dixon-Lewis, A computational model of the structure and extinction of strained opposed-flow premixed methane–air flames, in: 22nd Symposium (International) on Combustion, The Combustion Institute, 1989, pp. 1479–1494.
[26] G. Stahl, J. Warnatz, Numerical investigation of strained premixed Ch_4-air flames up to high pressures, Combust. Flame 85 (1991) 285.
[27] <http://www.fluent.com>.
[28] <http://w3.wtb.tue.nl/nl/organisatie/combustion_technology/flame-codes/chem1d/>.
[29] Alaa Omrane, Thermometry using laser-induced emission from thermographic phosphors: development and applications in combustion, Ph.D. thesis, Lund Institute of Technology, 2005.
[30] S.W. Allison, G.T. Gillies, Remote thermometry with thermographic phosphors: instrumentation and applications, Rev. Sci. Instr. 68 (7) (1997) 1–36.
[31] S.W. Allison, D.L. Beshears, T. Bencie, W.A. Hollerman and P. Boudreaux, Development of temperature sensitive paints for high temperature aeropropulsion applications, AIAA-2001-3528, 2001.
[32] <http://www.mathworks.com/access/helpdesk/help/techdoc/ref/pdepe.html>.
[33] M.J. Remie, Heat transfer from flames to a quartz plate, MSc. Thesis, Eindhoven University of Technology, Report no. WVT 2002.01, 2002.
[34] A. Bejan, Heat Transfer, John Wiley & Sons, Inc., 1993, ISBN 0-471-50290-1.